Optics Letters

Polarization-controlled orbital angular momentum of light passing through a cholesteric spherulite

A. N. Shalev,[1,2,*] A. A. Misura,[2] A. O. Georgieva,[2] A. V. Chernykh,[2] N. V. Petrov,[1,2,3] T. Orlova,[2,4] I. S. Lobanov,[2] E. V. Aksenova,[5] V. M. Uzdin,[2,5] and A. D. Kiselev[2]

[1]Qingdao Innovation and Development Center, Harbin Engineering University, Qingdao, Shandong 266000, China
[2]ITMO University, Saint Petersburg 197101, Russia
[3]School of Physics, Harbin Institute of Technology, Harbin, 150001, China
[4]Yerevan State University, Yerevan 0025, Armenia
[5]Saint Petersburg State University, Saint Petersburg 199034, Russia
*artem.shalev@metalab.ifmo.ru

Received 13 March 2025; revised 9 June 2025; accepted 16 June 2025; posted 17 June 2025; published 4 August 2025

By using a polarization-resolved common-path diffraction phase microscope coupled with a spin-to-orbit converter, we experimentally study two-dimensional in-plane distributions of amplitude and phase of light transmitted through a spherulite formed in a frustrated cholesteric liquid crystal cell. These distributions measured at different orientations of the output linear polarizer (analyzer) are used to obtain the orbital angular momentum (OAM) spectra characterizing the OAM content of the beam. The experimental data are found to be in good agreement with the theoretical results describing both the distributions and the OAM spectra based on an analytically designed model of toron-like localized liquid crystal structures. We show that the OAM spectrum can be controlled by changing the analyzer azimuth angle so that the dominant mode evolves between the limiting cases of the vortex mode with $l = -2l = -2$ and the vortex-free mode with $l = 0l = 0$.

https://doi.org/10.1364/OL.561669

A promising approach for the creation of tunable diffraction optical elements that control light polarization and phase is based on chiral nematic liquid crystals, also known as cholesteric liquid crystals (CLCs) [1]. CLCs are traditionally viewed as inhomogeneous anisotropic media whose unique combination of optical properties arises from the ground-state spiral (helix) orientational structure, which is highly sensitive to external stimuli. It is also known that, under certain conditions, frustrated cholesteric films with the CLC helix suppressed by the homeotropic boundary conditions may host a variety of localized chiral structures, in particular cholesteric spherulites, also known as cholesteric bubbles or torons.

According to [2], similar to q-plates [3], the interaction (the spin–orbit interaction) between the polarization (spin) and spatial (orbit) degrees of freedom of light propagating through the spherulites leads to the spin–orbit conversion [4] associated with the geometric phase [5] induced by inhomogeneous transformations of optical polarization. So, the spherulites can be regarded as micro-q-devices that exhibit geometric phase effects and thus possess remarkable achromatic properties over a wide wavelength range. Self-assembled arrays of spherulites act as two-dimensional diffraction gratings generating various controlled phase singularities in the diffracted laser beams [6].

Note that the spin–orbital interaction of light [7] originates from the properties of Maxwell's equations, and the optical angular momentum along with the geometric phase forms its underlying fundamental concepts. Under ideal settings, spin–orbit conversion is the process in which a circular polarized incident light beam acquires orbital angular momentum (OAM) and changes the sense of circular polarization to the opposite. This process arising from the spin–orbital interaction provides a tool for engineering structured light beams [8–10]. Among such beams, the vortex light-carrying OAM is promising for numerous applications ranging from tweezers to quantum computing [11].

In this Letter, our aim is to explore the concept of using torons as micro-q-devices and study the generation of reconfigurable OAM-carrying optical vortexes in the electromagnetic field transmitted through the localized CLC structure. To this end, we deal with the characterization of OAM, which requires knowledge of the phase distribution.

Experimentally, the small size of the spherulites leads to the expediency of observing the optical fields they form on a microscopic scale. Topological features of their structure, such as point defects and disclination lines, lead to the formation of spatially inhomogeneous polarization distributions, which suggest the use of polarimetric instruments. On the microscopic scale, the phase distribution formed by the torons in the far diffraction zone was observed in [2], while Fourier polarimetry [12] can be prospective for resolving the polarization states in this area. From the point of view of the diffraction theory, studying the evolution of the electromagnetic wave characteristics scattered by arrays and individual liquid crystal particles

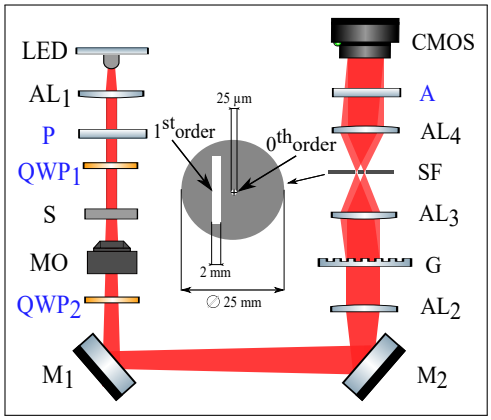

Fig. 1. Setup layout of the diffraction phase microscope coupled with the spin–orbit converter, which is mounted from the LED, achromatic lenses (AL_{1-41-4}), the polarizer (P), quarter-wave plates (QWP_{1-21-2}), the sample with cholesteric spherulites (S), the microscope objective (MO), mirrors (M_{1-21-2}), the diffraction grating (G), the spatial filter (SF), the analyzer (A), and the CMOS camera (C).

in the Fresnel diffraction region is also promising, since it provides more accurate information about the structural details of the sample. Although there have been several recent works on polarization-resolved digital holographic microscopy [13], the applied holographic setups have some limitations, such as vibration sensitivity, and the set of objects already studied is also limited. However, vibration resistance can be implemented using common-path interferometric setups such as diffraction phase microscopy [14].

In our experiments, we use an in-house polarization-resolved common-path diffraction phase microscope coupled with a spin-to-orbit converter to characterize the distribution of light scattered by torons in the Fresnel diffraction field and to trace the process of optical vortex formation. Our technique provides precise knowledge of the OAM mode content of the scattered light, thus opening up the possibility of analyzing spherulites as micro-vortex beams shapers. The experimental results are theoretically interpreted using the approach that combines the analytically designed model of the spherulite director field proposed in [15] and a numerical analysis of the electric field distributions of optical waves propagating through the CLC cell based on the well-known Jones matrix method.

Our experimental setup shown in Fig. 1 consists of two coupled optical systems: the diffraction phase microscope [16] and the spin-to-orbit converter for generating vortex beams [10]. The elements of the systems are indicated in black and blue fonts, respectively. The microscope setup used the point source light emitting diode (LED MTPS8065PT, Marktech Optoelectronics) with an irradiation wavelength of 650 nm and an emitting window diameter of 80 μm, which is sufficient to ensure high spatial coherence [17]. The light collimated by the achromatic lens (AL_{11}) is directed at the sample (S) and collected by the microscope objective (MO) with the magnification/numerical aperture equal to 40××/0.6. After MO, the light beam passes through the focus and expands. The optical path direction is inverted by two mirrors (M_{11} and M_{22}), and the expanded beam is collimated by the second lens (AL_{22}).

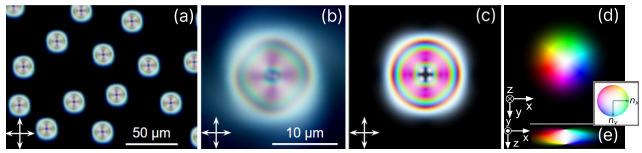

Fig. 2. (a) Experimentally taken white-light microscopic optical image of cholesteric spherulites (torons) under crossed-polarizer conditions formed in the initially frustrated CLC film, together with the (b) magnified view of a single toron and (c) a simulated optical image under the same illumination conditions. The director field distributions in the (d) *xy* and (e) *xz* planes obtained using the ansatz given by Eq. S3 in Supplement 1. The color palette in the inset in (d) and (e) represents the distributions of the director's azimuthal angle in the *xy* and *xz* planes. This color wheel depicts the southern hemisphere of director orientations, where n_z is negative. In the northern hemisphere, the colors become darker as n_z increases approaching the north pole with $n_z = 1$.

The amplitude diffraction grating (G) forms several diffraction orders that contain information about the spatial distribution of the optical characteristics of the sample. The diffraction orders are focused by the lens (AL_{33}) onto the spatial filter (SF), where the zeroth diffraction order is spatially filtered by the 25 μm diameter pinhole and converted into the reference wave, whereas the first diffraction order passes through the 2-mm wide slit aperture and serves as the object wave. All other diffraction orders are blocked. The lens (AL_{44}) collimates the diffraction orders and brings them together at an angle of 1.8°1.8° forming the off-axis hologram, which is captured by the complementary metal-oxide-semiconductor matrix detector (CMOS BFLY-U3-23S6M-C, Teledyne Imaging).

For the spin-to-orbit conversion, we used the Ix converter scheme shown in Fig. 2 of the review paper [10]. First, the linear polarization component of the diode emission is cut off by the polarizer filter (P). Then the quarter-wave plate (QWP_{11}) transforms the linearly polarized light into a circularly polarized beam, which illuminates the sample (S). The second quarter-wave plate (QWP_{22}), installed after the MO, converts the polarization vectors of the circular basis into linearly polarized modes. The linear polarization component is cut off or isolated by a rotary analyzer (A), which is capable to adjust and stabilize the linear polarization state.

Cholesteric spherulites and their assemblies can be created in frustrated CLC films by several methods, such as local perturbation of either the CLC orientational ordering or the CLC helical pitch value by illuminating the LC film with a laser beam [18,19], or by relaxation of the electrohydrodynamic instability caused by an applied external electric field [20], as well as by cooling from the isotropic CLC phase [21–22]. Here, we used the latter, simple and convenient method, to obtain a spatially disordered set of spherulites by heating a frustrated CLC film to the isotropic phase and subsequent rapid cooling.

The CLC consisted of the nematic LC HPC850600-100 (HCCH, China) doped with the chiral additive S-811 (Merck) at the concentration of $C = 0.84$ wt.%. The properties of HPC850600-100 are similar to those of the nematic LC E7; in particular, the ordinary and extraordinary refractive indices of HPC850600-100 are $n_o = 1.517$ and $n_e = 1.741$, respectively. The helical pitch measured using the Grandjean–Cano wedge was $p = 11.2$ μm. The obtained CLC was filled into a 10-μm thick LC sample (E.H.C., Japan) with homeotropic boundary

conditions on the confining glass substrates. Since the helical pitch slightly exceeded the cell thickness, the cholesteric helix was initially unwound, and the initial CLC state was uniformly homeotropic.

After heating the LC sample above the phase transition temperature into an isotropic liquid ($T_{N\to I} = 59°C$) and rapid cooling, many cholesteric spherulites were observed in the sample as shown in Fig. 2(a). Comparison of the cross-polarized optical image with those reported in [23] shows that the vast majority of the formed cholesteric spherulites can be identified as torons with an average diameter of 12 μm, which is comparable with the CLC film thickness. We chose a typical toron for further studies of its optical properties using a diffraction phase microscope.

As we mentioned above, orientational structure of the experimentally studied spherulite can be associated with torons. Similar toron-like structure of spherulites was also reported, e.g., in [2,18].

In order to model the three-dimensional structure of the spherulite, we utilize the method suggested in our previous study [15]. This method uses an analytical ansatz for the LC director field of a toron-like localized topological structure. According to this ansatz, the modeling process can be divided into three stages: (i) defining the vector field of the self-closed CLC helix, (ii) modifying the looped helix by adding a homeotropic structure multiplied by weight functions, and (iii) adding similarly organized structures to satisfy the reflection symmetry of spherulites. We describe the analytical design in more detail in Supplement 1.

In Fig. 2, we illustrate the resulting localized chiral structure, ≈12 μm in diameter, with two hyperbolic point defects (hyperbolic hedgehogs) on the z axis and one disclination line in the $z = 0$ plane. This is exactly the topology of a toron, which can be described as a skyrmion terminating at the two point defects so as to satisfy the homeotropic anchoring conditions [18].

All calculations were performed with the parameters listed in Table S1 in Supplement 1. Optical textures were computed for the paraxial optical field using the well-known Jones calculus formalism [24,25] to simulate the propagation of light through the CLC sample. According to this method, the CLC film is sliced into a set of thin slabs, and the effect of the jth thin slab is represented by a phase retardation plate with the optical axis directed along the CLC director varying in the lateral plane: $\mathbf{n}(x, y, j\Delta z) = (\sin\theta_j(x,y)\cos\phi_j(x,y), \sin\theta_j(x,y)\sin\phi_j(x,y), \cos\theta_j(x,y))$, where Δz is the slab thickness. The Jones vector of the transmitted light at each pixel of the computed polarized optical texture (image) is evaluated by successively multiplying the Jones matrices (see Eq. (5) in Ref. [15] for details).

Light passing through the cholesteric spherulite forms an optical vortex beam carrying OAM. It is known [26] that, in the paraxial approximation, the density of z (on-axis) projection of OAM is $l_z = \Im(E_x^* \partial_\phi E_x + E_y^* \partial_\phi E_y)$, where asterisk and ∂_ϕ stand for complex conjugation and derivative with respect to the azimuthal angle, respectively. For the special case of a scalar field E representing a linearly polarized component of the electric field, the expression for the OAM density can be reduced to the simplified form: $l_z = \Im E^* \partial_\phi E$.

Following [27–29], in order to analyze the angular momentum content of both simulated and experimental electric fields, we expand the complex-valued electric field E into a Fourier series over the angular harmonics and calculate the relative weighing of the power contained in each mode $P_l(z)\int_0^\infty |a_l(\rho,z)|^2 \rho d\rho / W$, where $W = \int dxdy|E|^2$. Since $J_z = L_z/W = \sum_l lP_l$ with $L_z = \int dxdyl_z$ gives the angular momentum per unit of energy, the distribution determined by the coefficients P_l will be called the OAM spectrum.

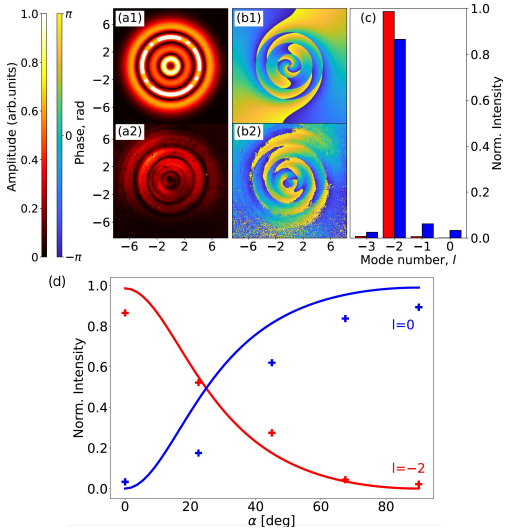

Fig. 3. (a1), (b1) Simulated and (a2), (b2) experimentally measured (a1), (a2) amplitude distributions, $|E|(x,y)$, and (b1), (b2) phase distributions at analyzer angle $\alpha = 0°$. (c) OAM spectra at analyzer angle $\alpha = 0°$. The simulated and experimental OAM are plotted in red (second tall bar) and blue (remaining bars), respectively. The white dashed line in (a1) denotes the boundary of the domain used to perform numerical integration in Eq. S5, Supplement 1. (d) Relative power weights of the vortex ($l = -2$) and vortex-free ($l = 0$) modes in the OAM spectrum as a function of the analyzer azimuth angle, α. Theoretical curves are shown as solid lines, and experimental data are shown as crosses.

In our experiments, the right-hand circular polarized wave with wavelength $\lambda = 650$ nm and the electric field vector $\mathbf{E}_{\text{in}} = (E_+^{(\text{in})}, 0)$ written in the circular basis passes through the toron, so that the transmitted light with $\mathbf{E}_{\text{out}} = (E_+^{(\text{out})}, E_-^{(\text{out})})$ generally acquires the left-hand circular polarized component and is no longer circular polarized. After the quarter-wave plate and the analyzer, whose optical axis is oriented along the direction specified by the azimuthal angle α, two-dimensional (2 D) distributions of the linearly polarized complex-valued component $E(x,y) = \cos\alpha E_-^{(\text{out})}(x,y) + \sin\alpha E_+^{(\text{out})}(x,y)$ are obtained by scanning the sets of digital holograms recorded at different values of the analyzer angle: $\alpha \in \{0°, 22.5°, 45°, 67.5°, 90°\}$. These distributions are then used to calculate both the amplitude, $A = |E|$, and the phase, $\phi = \arg E$, distributions shown in Figs. 3(a) and 3(b). The OAM spectra presented in Fig. 3(c) were calculated using Eqs. S4 and S5 in Supplement 1 and are shown for the harmonics with the azimuthal l number ranging from −3 to 0, since the contributions of all other modes are negligible.

Figures 3(a1) and 3(b1) also show the theoretical results. The simulated distributions are computed at $z = L$ using the Jones matrix method describing the propagation of light through the toron, the director field of which is modeled employing the ansatz from Eq. (S3) and the list of parameters from Table

S1 in Supplement 1. The simulated OAM spectra are evaluated by numerical integration over the domain that encircles the toron, and its boundary is indicated by the white dashed line in Fig. 3(a1).

The orientation of the analyzer (indicated as A in the setup depicted in Fig. 1) with $\alpha = 0°$ corresponds to the case of crossed polarizers. It can be seen that both the simulated (see Figs. 3(a1) and 3(b1)) and the experimental (see Figs. 3(a2) and 3(b2)) images show the vortex beam with the OAM spectrum dominated by the harmonics with $l = -2$ (see Fig. 3(c)). So, in our case, the component $E_{-}^{(\mathrm{out})}$ can be identified as a vortex-carrying part of the beam transmitted through the toron. Note that under perfect spin-to-orbit conversion [3,4], an incident light beam carrying spin angular momentum (SAM), $\mathbf{E}_{\mathrm{in}} = (E_{+}^{(\mathrm{in})}, 0)$, is transformed into an OAM-carrying vortex beam, $\mathbf{E}_{\mathrm{out}} = (0, E_{-}^{(\mathrm{out})})$, with inverted SAM.

The dynamics of the field conversion did not reveal any sharp discontinuities. When the analyzer is rotated from $\alpha = 0°$ to $\alpha = 90°$, we observe how the formation of a vortex-free light field occurs together with the evolution and annihilation of dipole pairs of the wavefront vortex phase dislocations [30]. The intensity of the vortex mode at $l = -2$ flows to the vortex-free mode at $l = 0$ with a slight blurring into the adjacent modes of the OAM spectrum (see Supplement 1 for more details). This effect implies the tunability of the OAM spectrum and is illustrated in Fig. 3(d). The range of angular harmonics in the spectrum is determined by the spatially variant birefringent nature of a toron [2]. It can be changed by varying the topology of the solitonic LC structure [23].

Referring to Fig. 3, the experimental data are in good agreement with the results of modeling. The amplitude and phase distributions are similar in topology. Since the determination of the vortex components (with circular symmetry) is extremely sensitive to the choice of spatial orientations of the light field, the inclination and decentering of the studied wavefront fields are primarily responsible for these deviations.

In conclusion, we have studied the concept of using torons as micro-q-devices producing electromagnetic fields with adjustable vortex and OAM content. The holographic approach was used to measure optical field distributions in the transverse plane, and diffraction phase microscopy demonstrated the possibility of qualitative recognition of phase distributions in microstructural polarization-phase elements. The experimentally obtained optical field amplitude and phase distributions are compared with the results of modeling assuming that the light propagates through the localized toron structure described by the analytical ansatz suggested in [15]. We have also analyzed both experimentally and theoretically the OAM spectra derived from the 2D distributions of the complex-valued amplitude of the output field, depending on the orientation of the analyzer axis (the linear polarizer placed at the end of the optical scheme). When the azimuth angle of the analyzer changes, the dominant modes of the OAM spectrum are found to evolve from the vortex mode with $l = -2$ to the vortex-free mode with $l = 0$ (see Fig. 3(d)). Thus, the OAM of the beam passed through the toron can be controlled by rotating the axis of the output linear polarizer. The simulated distributions and the OAM spectra are both found to be in good agreement with the experimental data. This fact substantiates the conclusion that the optical properties of the spherulite director field are adequately captured by our analytical model.

Funding. Ministry of Science and Higher Education of the Russian Federation (FSER-2025–0007, FSER-2025–0012).

Acknowledgment. AVC and NVP acknowledge state assignments (No. FSER-2025–0007 (experimental part)); ANS, ISL, and VMU acknowledge state assignments (No. FSER-2025–0012 (theoretical part)).

Disclosures. The authors declare no conflicts of interest.

Data availability. Data underlying the results presented in this paper may be obtained from the authors upon request.

Supplemental document. See Supplement 1 for supporting content.

REFERENCES

1. A. Ryabchun and A. Bobrovsky, Adv. Opt. Mater. **6**, 1800335 (2018).
2. B. Yang and E. Brasselet, J. Opt. **15**, 044021 (2013).
3. A. Rubano, F. Cardano, B. Piccirillo, *et al.*, J. Opt. Soc. Am. B **36**, D70 (2019).
4. L. Marrucci, C. Manzo, and D. Paparo, Phys. Rev. Lett. **96**, 163905 (2006).
5. K. Y. Bliokh, M. A. Alonso, and M. R. Dennis, Rep. Prog. Phys. **82**, 122401 (2019).
6. P. J. Ackerman, Z. Qi, and I. I. Smalyukh, Phys. Rev. E **86**, 021703 (2012).
7. K. Y. Bliokh, F. J. Rodríguez-Fortuño, F. Nori, *et al.*, Nat. Photonics **9**, 796 (2015).
8. L. Zhou, T. Zhong, Y. Liu, *et al.*, Adv. Funct. Mater. **34**, 2404614 (2024).
9. N. V. Petrov, B. Sokolenko, M. S. Kulya, *et al.*, Light Adv. Manuf. **3**, 640 (2022).
10. N. V. Petrov, B. Sokolenko, M. S. Kulya, *et al.*, Light Adv. Manuf. **3**, 752 (2022).
11. Y. Shen, X. Wang, Z. Xie, *et al.*, Light Sci. Appl. **8**, 90 (2019).
12. R. Röhrich, C. Hoekmeijer, C. I. Osorio, *et al.*, Light Sci. Appl. **7**, 65 (2018).
13. Y. Qiu, Z. Wang, Z. Weng, *et al.*, Appl. Opt. **62**, 7890 (2023).
14. Y. Jiao, M. E. Kandel, X. Liu, *et al.*, Opt. Express **28**, 34190 (2020).
15. I. Lobanov, E. Aksenova, T. Orlova, *et al.*, Symmetry **14**, 2476 (2022).
16. B. Bhaduri, C. Edwards, H. Pham, *et al.*, Adv. Opt. Photonics **6**, 57 (2014).
17. C. Edwards, B. Bhaduri, T. Nguyen, *et al.*, Opt. Express **22**, 5133 (2014).
18. I. I. Smalyukh, Y. Lansac, N. A. Clark, *et al.*, Nat. Mater. **9**, 139 (2010).
19. C. Loussert, S. Iamsaard, N. Katsonis, *et al.*, Adv. Mater. **26**, 4242 (2014).
20. P. J. Ackerman, J. van de Lagemaat, and I. I. Smalyukh, Nat. Commun. **6**, 6012 (2015).
21. S. Shvetsov, T. Orlova, A. Emelyanenko, *et al.*, Crystals **9**, 574 (2019).
22. M. G. Clerc, G. González-Cortés, and S. Echeverría-Alar, Phys. Rev. Res. **4**, L022021 (2022).
23. P. J. Ackerman and I. I. Smalyukh, Phys. Rev. X **7**, 011006 (2017).
24. P. Yeh and C. Gu, in *Optics of Liquid Crystal Displays* (Wiley, 1999), p. 438.
25. P. W. Ellis, E. Pairam, and A. Fernández-Nieves, J. Phys. D: Appl. Phys. **52**, 213001 (2019).
26. R. Zambrini and S. M. Barnett, Opt. Express **15**, 15214 (2007).
27. G. Molina-Terriza, J. P. Torres, and L. Torner, Phys. Rev. Lett. **88**, 013601 (2002).
28. I. A. Litvin, A. Dudley, and A. Forbes, Opt. Express **19**, 16760 (2011).
29. V. V. Kotlyar, A. A. Kovalev, and A. P. Porfirev, Opt. Express **27**, 11236 (2019).
30. A. Bekshaev, A. Chernykh, A. Khoroshun, *et al.*, Opt. Commun. **397**, 72 (2017).